Biomaterials 159 (2018) 1–12

Contents lists available at ScienceDirect

Biomaterials

journal homepage: www.elsevier.com/locate/biomaterials

Simultaneous three-dimensional visualization of mineralized and soft skeletal tissues by a novel microCT contrast agent with polyoxometalate structure

Greet Kerckhofs [a, b, *], Steve Stegen [b, c], Nick van Gastel [b, c], Annelies Sap [d], Guillaume Falgayrac [e], Guillaume Penel [e], Marjorie Durand [b, f], Frank P. Luyten [a, b], Liesbet Geris [b, g, h], Katleen Vandamme [b, i], Tatjana Parac-Vogt [d, 1], Geert Carmeliet [b, c, 1]

[a] Skeletal Biology and Engineering Research Center, Department Development and Regeneration, KU Leuven, Leuven, Belgium
[b] Prometheus, Division of Skeletal Tissue Engineering, KU Leuven, Leuven, Belgium
[c] Clinical and Experimental Endocrinology, Department of Clinical and Experimental Medicine, KU Leuven, Leuven, Belgium
[d] Molecular Design and Synthesis, Department of Chemistry, KU Leuven, Leuven, Belgium
[e] Univ. Lille, Univ. Littoral Côte d'Opale, EA 4490 - PMOI, F-59000, Lille, France
[f] Institut de Recherche Biomédicale des Armées, Department SMCF, F-91223, Brétigny-sur-Orge cedex, France
[g] Biomechanics Research Unit, Université de Liege, Liège, Belgium
[h] Biomechanics Section, Department of Mechanical Engineering, KU Leuven, Leuven, Belgium
[i] Biomaterials – BIOMAT, Department of Oral Health Sciences, KU Leuven, Leuven, Belgium

ARTICLE INFO

Article history:
Received 20 July 2017
Received in revised form
8 December 2017
Accepted 20 December 2017
Available online 22 December 2017

Keywords:
Contrast-enhanced computed tomography
Polyoxometalates
3D virtual histology
Bone marrow vasculature
Bone marrow adipocytes

ABSTRACT

Biological tissues have a complex and heterogeneous 3D structure, which is only partially revealed by standard histomorphometry in 2D. We here present a novel chemical compound for contrast-enhanced microfocus computed tomography (CE-CT), a Hafnium-based Wells-Dawson polyoxometalate (Hf-POM), which allows simultaneous 3D visualization of mineralized and non-mineralized skeletal tissues, such as mineralized bone and bone marrow vasculature and adipocytes. We validated the novel contrast agent, which has a neutral pH in solution, by detailed comparison with (immuno)histology on murine long bones as blueprint, and showed that Hf-POM-based CE-CT can be used for virtual 3D histology. Furthermore, we quantified the 3D structure of the different skeletal tissues, as well as their spatial relation to each other, during aging and diet-induced obesity. We discovered, based on a single CE-CT dataset per sample, clear differences between the groups in bone structure, vascular network organization, characteristics of the adipose tissue and proximity of the different tissues to each other. These findings highlight the complementarity and added value of Hf-POM-based CE-CT compared to standard histomorphometry. As this novel technology provides a detailed 3D simultaneous representation of the structural organization of mineralized bone and bone marrow vasculature and adipose tissue, it will enable to improve insight in the interactions between these three tissues in several bone pathologies and to evaluate the *in vivo* performance of biomaterials for skeletal regeneration.

1. Introduction

Histology is a highly valuable tool that contributes considerably to a better understanding of the normal and pathological processes in development and disease. It has a high discriminative power at the tissue and cellular level. However, sample preparation can be time-consuming and labor-intensive, certainly for bone, as it needs to be decalcified to allow certain immunostainings. In addition, histology shows limitations when analyzing the 3D spatial interrelations of different tissues and their local changes in pathological conditions. These shortcomings are mainly due to restricted sectioning orientation and often limited depth resolution. Confocal microscopy can address some aspects, as it provides 3D visualization of cells and tissues in thick histological sections [1,2], but the

* Corresponding author. Current address: Greet Kerckhofs, Biomechanics Lab, Institute of Mechanics, Materials, and Civil Engineering, UCLouvain, Belgium.
E-mail address: greet.kerckhofs@uclouvain.be (G. Kerckhofs).
[1] These authors have contributed equally and join the last authorship.

https://doi.org/10.1016/j.biomaterials.2017.12.016
0142-9612/

depth resolution is limited (~300 μm) and potential bleaching of the fluorophores may hinder analysis of large samples.

X-ray micro- and nanofocus computed tomography (micro- and nanoCT) can provide a solution, as it has been standardly used for 3D quantitative imaging of mineralized tissues [3–5]. This technology can also be used for soft tissue visualization, but requires the administration of a contrast agent when phase contrast imaging is not available. Two soft tissues that are highly connected to bone and that are important for bone metabolism, are bone marrow adipocytes and blood vessels. The adipocytes are considered to contribute to systemic energy metabolism [6], can function as a local energy reservoir and may influence hematopoiesis and osteogenesis [7]. However, the morphological parameters of the bone marrow adipocytes, such as the volume fraction, number and diameter, remain difficult to quantify. The second soft tissue is the bone vasculature, which closely interacts with bone cells. Indeed, the blood vessels not only provide oxygen and nutrients to the bone cells, but also osteoprogenitors that are critical for bone formation are localized adjacent to the blood vessels [8–11]. A detailed 3D visualization of the entire vascular network showing the complex organization in arteries, capillaries, sinusoids and veins is however lacking. Knowledge on the 3D morphology of the blood vessel network can provide a better understanding of the vascular organization, the probable blood flow and their possible impact on bone homeostasis.

Recent studies have focused on the use of X-ray opaque contrast agents for CT imaging of soft tissues [12,13]. Most of these contrast agents are, however, used for (*in vivo*) perfusion of the tissues of interest, rather than for effectively staining the different subparts. Indeed, several X-ray opaque contrast agents are available to image blood vessels after perfusion [14–17]. The perfusion technique has, however, several shortcomings including (i) the potential need for dual energy scanning or a two-step scanning protocol when assessing them in bone, i.e. before and after bone decalcification [18] and (ii) the limited perfusion of the capillaries and sinusoids, where the flow velocity is assumed to be low [16]. On the other hand, to effectively stain soft tissues through immersion, several X-ray opaque contrast agents are available for the following tissues: extracellular matrix [19], cartilage [20–28], adipocytes [29–31] and connective tissues [32,33]. Limitations of osmium tetroxide staining, which is the most commonly used staining technique for bone marrow adipocytes [29–31], are the toxicity and the two-step scanning protocol. In addition, most of the existing contrast agents are destructive [34–36] or toxic, preventing subsequent (immuno)histological assessment. Iodine potassium iodide (I_2KI), for example, stains different types of soft tissues, but causes substantial soft tissue shrinkage dependent on the concentration, staining time and tissue structure/composition [34]. Also phosphotungstic acid (PTA) introduces shrinkage of brain and muscle tissue, although to a lesser extent than I_2KI [35]. However, using contrast-enhanced microCT (CE-CT) data for morphometric and volumetric analyses requires absence of shrinkage and tissue deformation. Also, subsequent histological analysis highly depends on preservation of immunoreactivity. Finally, knowledge of the tissue-specific binding mechanisms of many existing contrast agents is limited [32,37].

In this study, we aimed to develop, test and validate a novel contrast agent for staining soft skeletal tissues that does not alter the tissue structure or immunoreactivity (i.e. having a neutral pH in solution), and that is to be used for *ex vivo* CE-CT purposes. We therefore evaluated two different polyoxometalate (POM) formulations. The first one, PTA, has been reported to visualize soft tissues in combination with mineralized bone using microCT, and is described to bind to fibrin, collagen, and fibers of connective tissues [26,32,35,37]. However, PTA is one of the strongest acids among the polyoxometalates [38] and thereby induces significant tissue shrinkage, which strongly affects tissue integrity [19,35]. The other POM-formulation, an Hafnium-substituted Wells-Dawson POM (Hf-POM), has its main application as catalyst [39–41], and has not yet been used as contrast agent for micro- or nanoCT imaging. Hf-POM is known to be stable under physiological pH and temperature and is used in the form of a salt, which makes it potentially less destructive than PTA. Here, we first used Raman spectroscopy to get a better understanding of the binding mechanisms of the two POMs, which is crucial for correct interpretation of the CE-CT images. Next, we showed the possibility to perform immunohistochemistry after staining with Hf-POM, but not with PTA, and the strong correlation between histology and Hf-POM-based CE-CT analysis in quantifying blood vessels and adipocytes. Moreover, we highlighted, using murine long bones a blueprint, that Hf-POM-based CE-CT allows quantification of the 3D morphological parameters as well as the spatial distribution of the different skeletal tissues in relation to each other during normal bone homeostasis as well as in aging and diet-induced obesity. Taken together, we present a novel contrast agent for CE-CT that (i) has similar binding mechanisms to soft tissues as PTA but has a neutral pH in solution, (ii) is stable under physiological pH and temperature, (iii) does not alter the tissue integrity of the stained samples, and (iv) enables subsequent (immuno)histological processing and staining. Moreover, it allows simultaneous 3D multi-tissue visualization and characterization of different skeletal tissues, namely mineralized bone, bone marrow vasculature and adipose tissue, and this without the need for perfusion of the contrast agent.

2. Materials and methods

2.1. Mice

All animal experiments were performed in accordance with the Belgian legislation and were approved by the Ethical Committee of the Faculty of Biomedical Sciences of the KU Leuven. Male C57Bl/6Rj mice were obtained from Janvier SAS (France) and were used in two studies: in a 'validation of the contrast agents' study to analyze the correlation between POM-based CE-CT and histology; and in a bone pathology study to investigate the added value of the POM-based CE-CT compared to histomorphometry. For the validation of the contrast agents, the two POMs were analyzed on tibias from 4-week-old mice and compared to unstained control samples ($n = 3$ per group). In the bone pathology study, three groups were used. 8- and 30-week-old mice (YNG and OLD respectively; $n = 8$) were compared to analyze the effect of aging. In addition, 8-week-old mice were fed a high fat diet (HFD) for 22 weeks (HFD, $n = 8$; 60% energy as fat, Ref No D12492, Open Source Diets, Research Diets Inc., USA). All animals were euthanized and the tibias were harvested, fixed in a 2% paraformaldehyde solution (Sigma Aldrich, USA) for 16 h and stored in phosphate-buffered saline (PBS) at 4 °C. Before POM-staining, the distal end of the bones was removed to allow better diffusion of the contrast agent into the bone marrow compartment.

2.2. Contrast agents

Two different POM formulations were tested, namely PTA ($H_3PW_{12}O_{40}$) and Hafnium-substituted Wells-Dawson POM ($K_{16}[Hf(\alpha_2\text{-}P_2W_{17}O_{61})_2]\bullet 19H_2O$), further referred to as PTA and Hf-POM respectively. The Hf-POM has a net charge of −16 (the metal ion has a +4 charge and the polyoxometalate scaffold has a charge of −20). PTA has a molecular weight (MW) of 2880.2 g/mol, while the MW of the Hf-POM is 9472.73 g/mol. Consequently, in terms of size, Hf-POM is approximately four times larger compared to PTA.

POMs were used at following concentrations: PTA at 25 mg/ml PBS [19] and Hf-POM at 35 mg/ml PBS. For the latter, we noticed that a concentration of 25 mg/ml PBS was insufficient for proper tissue staining, whereas 35 mg/ml PBS was identified as the lowest possible concentration for sufficient contrast difference between the soft tissues. Samples were incubated in the staining solution during 48 h at 4 °C while shaking gently (see Supplementary Fig. S1 for the determination of the optimal staining time).

2.3. Raman spectroscopy

2.3.1. Sample preparation

Raman spectroscopy was used to get a better understanding of the binding mechanisms and to provide an indication for the binding efficiency of the different POMs to collagen type I (Coll-I; C7774 - Sigma Aldrich), collagen type II (Coll-II; C1188 - Sigma Aldrich), fibrin (F5386 - Sigma Aldrich) and rat tendon. First, Raman analysis was performed on the POM powders, proteins and rat tendon separately to obtain reference spectra of each compound. Then, the proteins and the rat tendon were incubated overnight in the POM solutions, after which they were rinsed shortly in deionized water (first rinsing step – to remove unbound solution) and dried at room temperature. Raman spectroscopy on the dried samples was performed to gain a better understanding of the binding mechanisms between the POMs and the proteins/tendon. Finally, the dried samples were again rinsed in deionized water overnight (i.e. 'second rinsing step'), followed by drying. Samples were again analyzed by Raman spectroscopy and the difference between the measurements before and after the second rinsing step allowed us to get an indication of the binding affinity of the POMs to the proteins/tendon.

2.3.2. Acquisition

Spectra were acquired with a Raman microspectrometer LabRAM HR800 (HORIBA, France) [42,43]. Ten spectra were acquired for each sample with an integration time of 60 s and two accumulations. The spectral range was 300–1800 cm^{-1} with a resolution of 4 cm^{-1}. All Raman spectra were processed using Labspec software (HORIBA). A Savitzky-Golay smoothing filter (filter width: 3; polynomial order: 2) was applied on all spectra.

2.3.3. Signal processing to get an indication of the binding affinity

To get an indication of the affinity of the two POMs to the proteins/tendon, we made use of the intensity ratios [44] of the peak specific for the POMs and the peak specific for the proteins/tendon (i.e. Amide III - 1186-1300 cm^{-1}). The intensity of each peak was integrated over defined Raman shift regions in the spectrum using a sum filter. The filter calculates the intensities within the chosen borders and the background is subtracted by taking the baseline from the first to the second border [45]. The intensity ratios (R) were calculated according to the following peaks: Hf-POM (933-1002 cm^{-1})/Amide III (1186-1300 cm^{-1}); PTA (957-1033 cm^{-1})/Amide III (1186-1300 cm^{-1}). The difference between the intensity ratios before and after the second rinsing step was expressed relative to the intensity ratio before the second rinsing step as follows:

$$\Delta = \frac{R^{before} - R^{after}}{R^{before}} \times 100$$

where R^{before} is the intensity ratio for the POM determined before the second rinsing step; R^{after} is the intensity ratio for the POM determined after the second rinsing step, and Δ gives an indication of the affinity of the POM. The intensities of all the peaks, as well as the intensity ratios were calculated using the PLS toolbox (v8.2, Eigenvector Research, Inc., USA) and a custom-developed script in Matlab R2016b (Mathworks Inc, Natick, USA).

2.4. Contrast-enhanced high resolution microfocus computed tomography (CE-CT) - acquisition

Samples were imaged using a Phoenix NanoTom S (GE Measurement and Control Solutions, Germany) [5,46]. Because of the relatively high X-ray attenuation of the POM-stained samples, a diamond-coated tungsten target was applied. The system was operated at a voltage of 70 kV and a current of 60 μA, and a 0.3 mm filter of aluminum was used to reduce beam hardening during the acquisition. The exposure time was 500 ms, and 2400 images were acquired over 360° using the fast scan mode (frame averaging = 1; image skip = 0) [46]. These settings allowed limitation of the scanning time to 20 min to avoid heating of the sample during scanning. The proximal tibiae were examined at 2 μm isotropic voxel size to assess the morphological parameters of the trabecular bone and the bone marrow adipocytes and vasculature in the metaphysis. During reconstruction (Datos|x, GE Measurement and Control Solutions), we applied a beam hardening correction of 7 and a Gaussian filter of 6.

2.5. Histology

Tibias were decalcified for 2 weeks in a 0.5 M EDTA/PBS solution and embedded in paraffin. 6 μm-thick sections were stained with hematoxylin and eosin (H&E) for visualization of the bone and bone marrow adipose tissue, whereas blood vessels were visualized using CD31 immunostaining [47,48].

2.6. Contrast-enhanced high resolution microfocus computed tomography (CE-CT) – image processing and analysis

2.6.1. Validation of the contrast agents – comparison between CE-CT and (immuno)histology

To validate whether the POM staining visualizes blood vessels and adipocytes correctly, we thoroughly compared these structures as detected on the histological sections versus corresponding CE-CT images. To this end, we used DataViewer (Bruker MicroCT, Belgium) for the reorientation of the CE-CT datasets and an in-house developed MatLab tool for the reconstruction of the CE-CT image at the same cutting angle as the histological section [49]. After a visual evaluation of the features of interest (i.e. blood vessels or adipocytes) in the histological sections compared to the corresponding CE-CT images, a region of interest (ROI) was selected in each 2D section, in which the number of blood vessels (on CD31 stained sections) or adipocytes (on H&E stained sections) was counted.

2.6.2. Bone pathology study - morphological assessment of mineralized bone

For the assessment of the trabecular bone morphology in the metaphysis of the tibias, CTAn (Bruker MicroCT) was used. 500 images (covering 1 mm height) were selected starting at the growth plate level. This specific region was chosen to allow simultaneous evaluation of the changes in the bone, bone marrow adipose tissue and vasculature, and to have an unbiased view on the interrelation of these different tissues. On the 500 images, a volume of interest (VOI) was selected which includes the trabecular bone, but not the cortical bone. Then, using automatic 3D Otsu segmentation, the images were binarized, and noise was removed by a closing operation and a double despeckling step [46]. Using 3D analysis, the trabecular bone volume in the total VOI (BV/TV - %) and the trabecular number (Tb.N. – mm^{-1}), thickness (Tb.Th. - μm)

and separation (Tb.Sp. - μm) were quantified. The 3D thickness distribution is based on the model-independent technique from Hildebrand and Ruegsegger [50]. CTVox (Bruker MicroCT) was used for 3D visualization of the binarized images of the bone.

2.6.3. Bone pathology study - morphological assessment of adipocytes and vasculature

The bone marrow adipocytes and vasculature were assessed in the same VOI as where the trabecular bone morphology was measured. The medullar open volume (MV) was calculated as the VOI minus the volume of trabecular bone. Manual global thresholding was used to segment the adipocytes, the blood vessels and the remaining (hematopoietic) tissue. The threshold values were chosen at the intersection of two neighboring peaks, as indicated in Supplementary Fig. S2. Although both the adipocytes (hydrophobic) and the blood vessels (only containing few red blood cells) were not stained by the Hf-POM, they had distinct grey-levels (Supplementary Fig. S2), and thus could be segmented separately. First, a binarization of the adipocytes was performed, and individual adipocytes touching neighboring ones were separated using an opening operation (round kernel, radius 1, 3D space). Then, noise was removed by a closing and a double despeckling step. Based on 3D analysis, the adipocyte density (#/mm^3 MV) and volume fraction in the MV (%) were determined. Since adipocytes are sphere-shaped, the thickness, measured as described above [50], reflects the true diameter of the adipocytes, and thus allowed us to determine the adipocyte diameter (μm) distribution.

To quantify the blood vessels, the original grey-scale images were reloaded, but the VOI was replaced by an adapted VOI, being the previous VOI minus the dilated (2 voxels) binary phase of the adipocytes to eliminate partial volume effect artefacts. Subsequently, the images were binarized for the blood vessels, and two closing operations were performed (round kernel, radius 4 and 6 respectively, 3D space) with an intermediate despeckling step (removal of white speckles, 3D space, less than 1050 voxels). Finally, a last despeckling step (removal of white speckles, 3D space, less than 5500 voxels) was performed to remove non-connected blood vessels (<5% of the total blood vessel volume) that were present due to the limited spatial image resolution. 3D analysis allowed calculating the blood vessel number (mm^{-1}), thickness (μm) distribution and volume fraction in the MV (%). 3D visualization of the adipocytes and blood vessels was performed using CTVox (Bruker MicroCT).

2.6.4. Branching analysis vascular network

To analyze the 3D branching of the bone marrow vasculature, BoneJ was used [51–53]. Briefly, the binarized images of the bone marrow vasculature were loaded into Fiji [54] and topology-preserving medial axis skeletons were generated using the 'Skeleton 3D' plugin [52,53]. The 'Analyze skeleton' plugin allowed calculating the total number of branches and the mean branch length (μm).

2.7. Statistical analysis

Analysis of normality of the data was performed by using the Shapiro-Wilk test and the potential presence of outliers was evaluated using the Dixon test. Equality of variances was assumed when the F-test revealed values of $p > .05$. For the comparison between histology and CE-CT, a paired *t*-test was applied. For the 3D analysis, the HFD group and YNG group were both independently compared to OLD animals by using a two-tailed unpaired *t*-test with equal or unequal variance depending on the F-test. All statistical analyses were performed using Microsoft Excel, AnaStats and/or GraphPad Prism.

3. Results and discussion

3.1. Binding mechanisms and affinity – Raman spectroscopy

To obtain simultaneous 3D visualization of the different tissue components of the bone without interfering with subsequent immunohistochemistry, we evaluated two different POM formulations. For correct interpretation of the CE-CT images, more insight into the binding mechanisms and the binding efficiency of the different POMs is crucial. To this end, we used Raman spectroscopy. Fig. 1 shows the reference Raman spectra of the two POMs, the three proteins and the rat tendon in the spectral window of 400–1800 cm^{-1}. The main peaks of Hf-POM and PTA were found at 964 and 978 cm^{-1}, and 989 and 1007 cm^{-1}, respectively. These peaks were assigned to the symmetric and asymmetric vibrations of the tungsten-to-oxygen double bond [55,56]: ν_s and ν_{as} W=O. The two Raman spectra also had characteristic bands in the 300-900 cm^{-1} range, but no assignment was found in literature. The Raman spectrum of PTA was in agreement with published data [57]; the peak at 917 cm^{-1} was assigned to asymmetric stretching vibration of W-O_c-W (O_c is the corner sharing bridging oxygen atom; W is tungsten) [55]. The reference Raman spectra of Coll-I, Coll-II, fibrin and rat tendon were in agreement with previous studies [58–61].

To get a better understanding of the binding mechanisms of the POMs, Raman spectroscopy was performed after overnight incubation of the proteins and rat tendon in the two different POMs. The Raman spectra of the Hf-POM-stained Coll-I revealed a

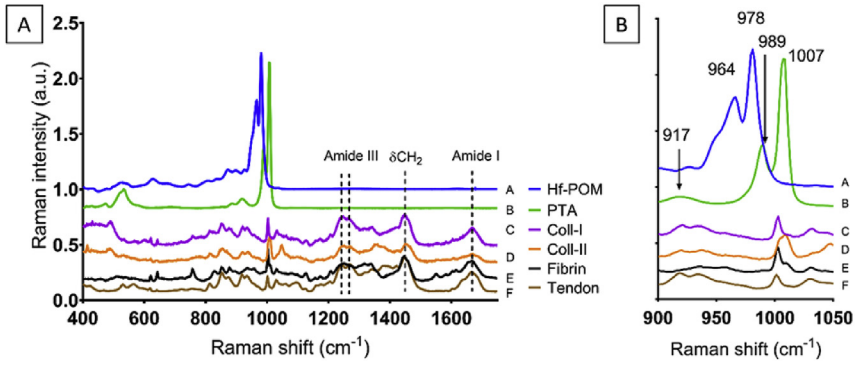

Fig. 1. Reference Raman spectra of the POMs, proteins and tendon. (A) Raman spectra of Hf-POM, PTA, Coll-I, Coll-II, fibrin and rat tendon and (B) a zoom of (A) within the range of 900–1050 cm^{-1}.

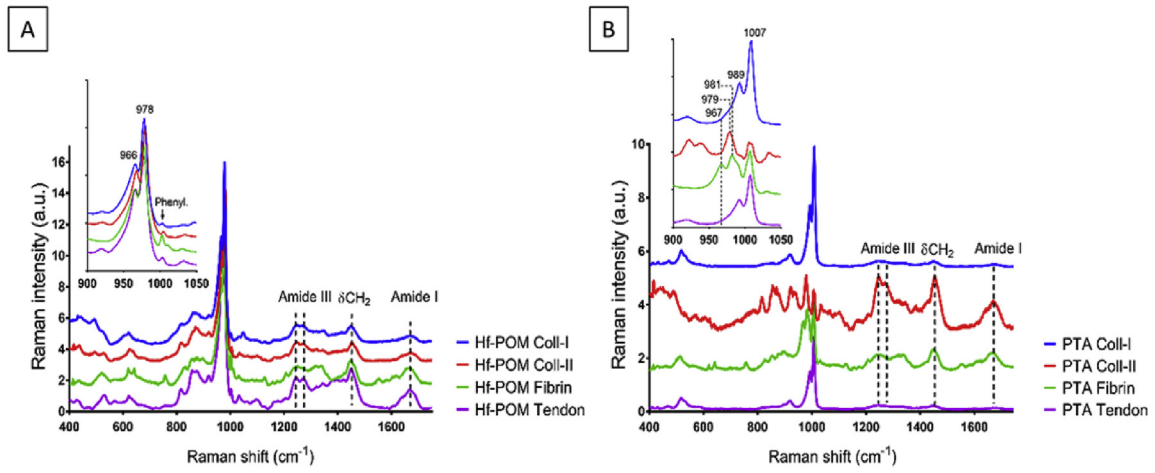

Fig. 2. Raman spectra of Hf-POM-stained and PTA-stained proteins and tendon. Raman spectra of (A) Hf-POM-stained Coll-I, Coll-II, fibrin and rat tendon and of (B) PTA-stained Coll-I, Coll-II, fibrin and rat tendon. Phenyl.= Phenylalanine.

combination of peaks that were assigned to the Hf-POM (966 and 978 cm^{-1}) and to the Coll-I (Phenylalanine 1001 cm^{-1}, Amide III 1247 and 1270 cm^{-1}, δCH_2 1450 cm^{-1}, and Amide I 1670 cm^{-1}) (Fig. 2A). Comparison with reference Raman spectra of Hf-POM and Coll-I (Fig. 1) showed no shift in characteristic peaks of Hf-POM and Coll-I. Similar results were obtained for Hf-POM-stained Coll-II, fibrin and tendon (Fig. 2A).

The Raman spectra of PTA-stained Coll I or tendon showed peaks that were assigned to PTA (989 and 1007 cm^{-1}) and Coll-I or tendon (Fig. 2B), with no shifts in these characteristic peaks. Raman spectra of the PTA-stained Coll-II showed peaks of Coll-II and PTA, which were not shifted, but also an additional peak at 981 cm^{-1} (Fig. 2B). Also for PTA-stained fibrin, new peaks were observed (967 and 979 cm^{-1}) that did not match with the reference spectra (Fig. 2B).

Since the positions of the characteristic peaks of the Hf-POM, the proteins and the rat tendon were not modified after staining, two main conclusions are drawn: (i) the Hf-POM-staining does not alter the chemical structure of the proteins or the rat tendon and (ii) the bonds between the Hf-POM and the proteins or tendon are electrostatic. These conclusions are supported by a previous study on POMs and the protein sex determining region Y-box 2 (SOX2) [62]. Similar conclusions are drawn for PTA-stained Coll-I and tendon. However, in case of PTA-stained Coll-II and fibrin, new unidentified peaks appeared after PTA-staining, indicating a possible alteration of the chemical structure of the proteins or of PTA, or the formation of a new compound.

Finally, we obtained an indication of the affinity of the two POMs by determining the relative differences in intensity ratio (Δ) between the POM-specific peak and the protein/tendon-specific peak before and after the second rinsing step (Table 1). Hf-POM showed a decrease in Δ of −11% for the tendon, going to −37% for Coll-II, which indicates that the relative amount of Hf-POM fixed to the tendon or Coll-II decreased after washing with 11% and 37% respectively. For PTA, we could only obtain an indication of the affinity to tendon and to Coll-I, since the characteristic peaks of PTA disappeared for PTA-stained Coll-II and fibrin. Based on these results, we could conclude that no major difference was observed in the affinity of the two POMs for tendon and Coll-I. However, PTA does alter the chemical structure of fibrin and Coll-II, confirming its destructive character.

Table 1
Indication of the affinity of the POMs. Difference in the intensity ratios (Δ) between the POM-specific peak and the protein/tendon-specific peak before and after the second rinsing step.

	Coll-I	Coll-II	Fibrin	Rat tendon	*Average*
Hf-POM	−36%	−37%	−29%	−11%	*−28 ± 12%*
PTA	−27%	/	/	−28%	*−28 ± 0.70%*

3.2. Validation of the contrast agents – comparison between CE-CT and (immuno)histology

After having obtained a better insight into the binding mechanisms of the different POMs, we assessed whether the use of POMs still allowed histological analysis after CE-CT analysis, as the possibility to use several methodologies on one sample would be an important advantage. To this end, we used murine long bones as blueprint. We first stained tibias with one of the two POMs and scanned them using CE-CT (Fig. 3A and D). Importantly, for CE-CT no specific sample preparation, such as decalcification, was required. After CE-CT imaging, samples were decalcified, embedded and sectioned, followed by CD31 immunostaining to visualize blood vessels (Fig. 3B) or H&E staining to visualize adipocytes (Fig. 3E). PTA staining prohibited CD31 staining and resulted in faint H&E staining (data not shown), while the Hf-POM allowed excellent CD31 and H&E staining, comparable to unstained control samples. These data indicate that Hf-POM can be used as a novel CE-CT contrast agent for biological tissues that is moreover non-destructive and allows histological evaluation afterwards.

Because of the non-destructive character of Hf-POM, a one-on-one quantitative comparison between the CE-CT images (Fig. 3A and D) and the corresponding histological sections (Fig. 3B and E) was possible. The number of blood vessels (Fig. 3C) and adipocytes (Fig. 3F) quantified in the two types of images was highly comparable, resulting in a strong correlation between Hf-POM-based CE-CT and histology (Spearman correlation of 0.8 and 0.9 for adipocyte number and blood vessel number, respectively). Moreover, visual evaluation of the corresponding images of Hf-POM-based CE-CT and histology showed that both technologies detected the same morphology and distribution of the blood vessels (Fig. 3G and H) and adipocytes (Fig. 3I and J), further emphasizing the accuracy and validity of the CE-CT analysis.

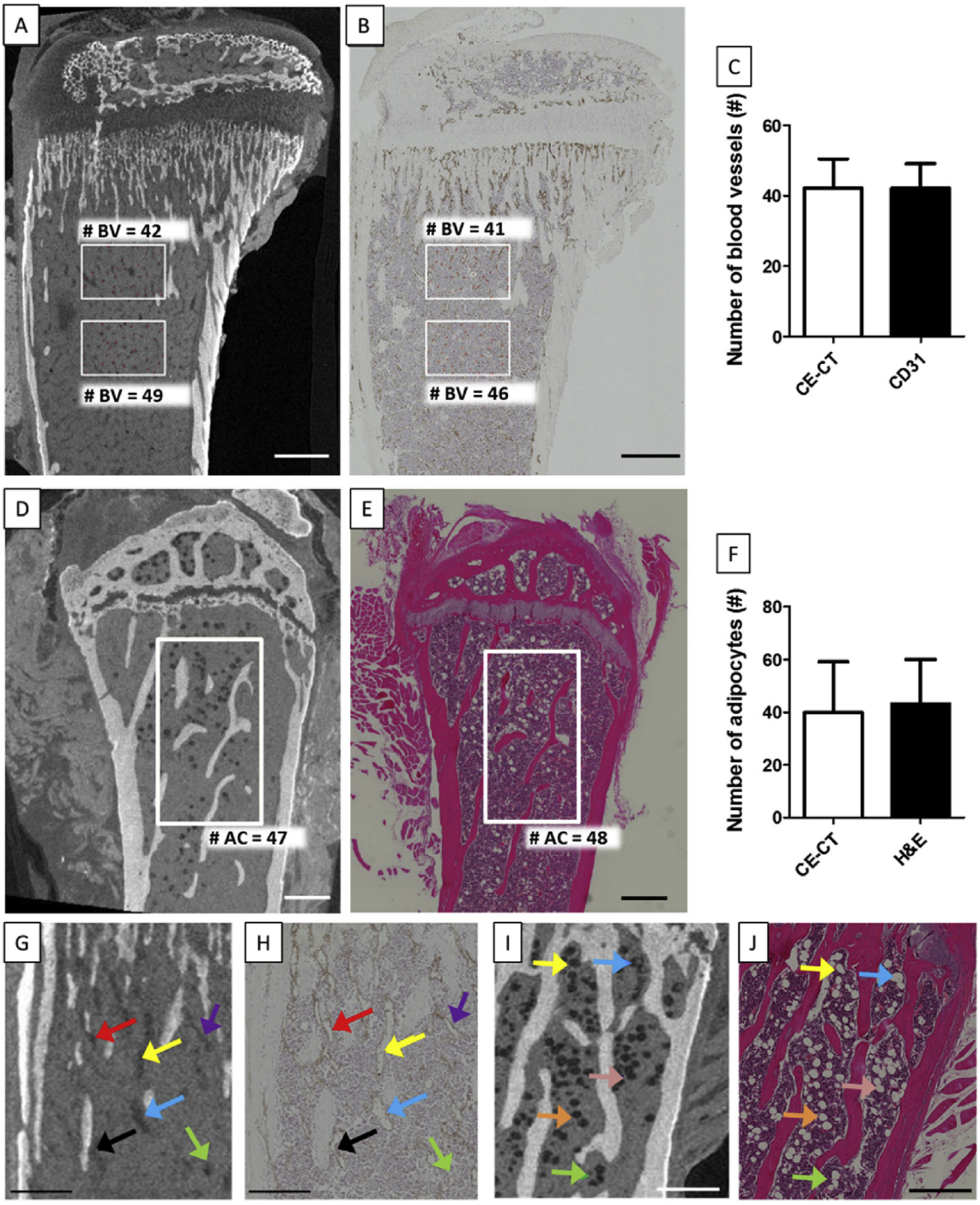

Fig. 3. Validation of Hf-POM-based CE-CT by comparison to histology. (A) Coronal CE-CT image of a tibia stained by Hf-POM, and (B) the corresponding immuno-histological CD31-stained section visualizing blood vessels. BV = blood vessels. Scale bars = 250 μm. (C) Quantitation of the blood vessel density (#/mm^2) in the CD31-stained histological sections and the corresponding CE-CT images within the white ROIs ($n = 3$; 6 sections per sample). Data are represented as average + standard deviation (SD). A paired t-test was used for statistical analysis. (D) Coronal CE-CT image of a tibia stained by Hf-POM, and (E) the corresponding H&E-stained section. AC = adipocytes. Scale bars = 250 μm. (F) Quantitation of the adipocyte density (#/mm^2) in the H&E-stained histological sections (white dots) and the corresponding CE-CT images (dark dots) within the white ROIs ($n = 3$; 6 sections per sample). Data are represented as average + SD. A paired t-test was used for statistical analysis. (G and H) are zooms of A and B respectively; and (I and J) zooms of C and D respectively, with the colored arrows indicating corresponding structures in both images. Scale bars = 100 μm.

3.3. Bone pathology study - 3D morphological quantification of the different skeletal tissues in long bones

After determining the accuracy and validity of Hf-POM-based CE-CT, we next investigated whether its use provided unique information, including insight in cell-specific characteristics, intertissue relationships and regional 3D analyses, which would highlight the added value of this technique. To this end, we performed 3D image analysis of the CE-CT datasets in mouse models of two well-established bone pathologies, namely aging and diet-induced obesity, which are claimed to affect not only bone mass but also its vascularity and adiposity [46,63,64].

3.3.1. Morphological assessment of the trabecular bone

Because there is no need to decalcify the bone before CE-CT imaging, we were able to assess the 3D morphology of the mineralized bone within the Hf-POM-based CE-CT datasets and thus we investigated the changes in trabecular bone morphology in response to aging or a high fat diet. Although aging did not result in decreased BV/TV (Fig. 4A), 30-week-old mice had significantly less (Fig. 4D), but thicker trabeculae (Fig. 4) that were more separated from each other (Fig. 4C) compared to the 8-week-old mice. This age-induced trabecular bone phenotype corresponds well with the reported age-related skeletal changes [65,66]. On the other hand, the HFD-fed mice had significantly less (Fig. 4D) and wider spread (Fig. 4C) trabeculae, resulting in significantly decreased BV/TV (Fig. 4A). Similar effects of HFD on BV/TV and trabecular number were described in earlier studies [63,67–71], although the response in trabecular thickness varied between studies, possibly due to different sites of analysis [46,63,64,71].

3.3.2. Morphological assessment of the bone marrow adipocytes

Apart from bone, we analyzed, within the same datasets, whether Hf-POM-based CE-CT analysis allowed the characterization and quantification of the bone marrow adipocytes, given the fact that single adipocytes could be detected with high contrast and spatial resolution as shown in the validation of the contrast agents. Hf-POM-based CE-CT analysis showed clear differences in the bone marrow adipose tissue between the three groups (Fig. 5A–C). Aging induced a significant increase in the bone marrow adipocyte volume fraction (8.9-fold; Fig. 5D), adipose density (5.3-fold; Fig. 5F) and average adipocyte diameter (1.6-fold; Fig. 5E). This effect corresponds well with the literature, reporting an aging-associated increase in the bone marrow adiposity [72,73]. Different from most published data, we were now also able, because of the high spatial and contrast resolution of our images, to quantify the morphological parameters of individual adipocytes, such as the true adipocyte diameter and its distribution (measured in 3D). We observed that aging resulted in a significant increase in the average adipocyte diameter.

Feeding mice a high fat diet during 22 weeks further increased the volume fraction of adipocytes (4.4-fold; Fig. 5C), as has been previously reported [73–75]. However, we now show that this higher value is mostly due to an increase in the average adipocyte diameter (1.4-fold; Fig. 5E) rather than in the density of adipocytes (Fig. 5F).

3.3.3. Morphological assessment of the bone marrow vascularization

Next, we observed that Hf-POM-based CE-CT analysis allowed 3D visualization, with high contrast and spatial resolution and within the same datasets, of the entire vascular network in the medullar space. Moreover, Hf-POM-based CE-CT analysis revealed clear differences in the bone marrow vasculature between the three groups (Fig. 6A–C). Although aging did not have a significant effect on the general morphological parameters of the blood vessels, such as the blood vessel volume fraction (Fig. 6D), the average blood vessel thickness (Fig. 6E) or the blood vessel number (Fig. 6F), it altered the 3D spatial organization and the branching of the blood vessel network (Fig. 6A–B). More specifically, the average branch length decreased significantly with aging (1.3-fold; Fig. 6H).

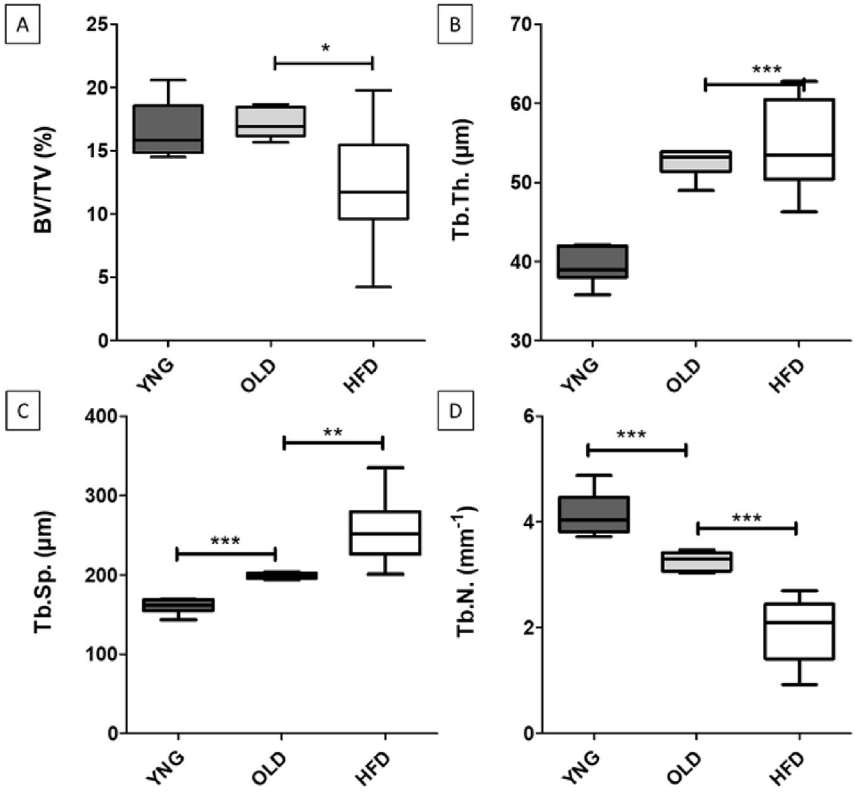

Fig. 4. Quantitative morphological assessment of the trabecular bone. CE-CT-based (using Hf-POM) analysis of the (A) BV/TV, (B) Tb.Th., (C) Tb.Sp. and (D) Tb.N. for the YNG, OLD and HFD groups. $n = 7 - 8$ *per group.* $^{*}p < .05$, $^{**}p < .01$, *and* $^{***}p < .001$. Data are represented in a box plot as median ± min/max. The HFD group and YNG group were both independently compared to OLD animals by using a two-tailed unpaired *t*-test.

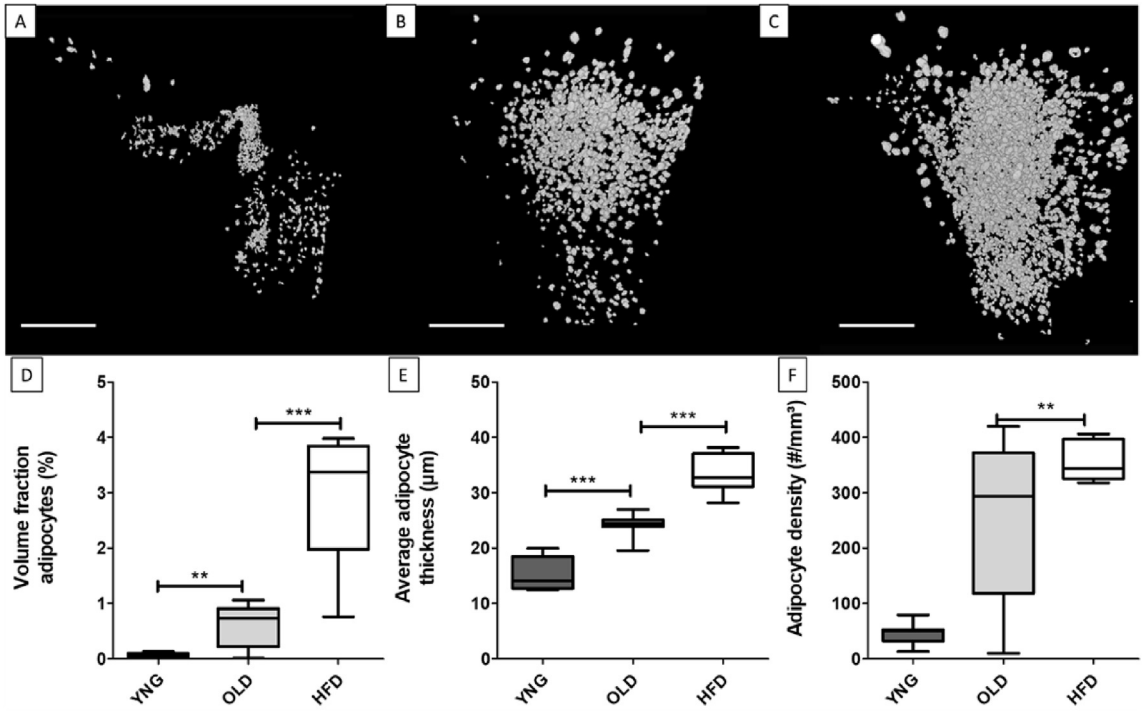

Fig. 5. Quantitative morphological assessment of the bone marrow adipocytes. Representative 3D visualization, using Hf-POM-based CE-CT, of the adipocytes in the bone marrow compartment of the tibial metaphysis (1.2 mm height) of (A) YNG, (B) OLD and (C) HFD mice. Scale bars = 250 μm. Quantification of the (D) volume fraction of the adipocytes in the MV, (E) average adipocyte diameter and (F) adipocyte density for the YNG, OLD and HFD groups. $n = 7 - 8$ *per group.* $^{**}p < .01$, *and* $^{***}p < .001$. Data are represented in a box plot as median ± min/max. The HFD group and YNG group were both independently compared to OLD animals by using a two-tailed unpaired *t*-test.

Importantly, this effect can only be detected by 3D imaging techniques such as CE-CT, as standard histology is mostly limited to 2D analysis and thus precludes full 3D branching analysis of the entire blood vessel network.

The high fat diet did not alter the bone marrow blood vessel volume fraction (Fig. 6D) manifestly, but it did increase the average blood vessel thickness (2.7-fold; Fig. 6E) and decrease the blood vessel number (3.9-fold; Fig. 6F) significantly. The distribution of the blood vessel thickness (Fig. 6I), measured in 3D, showed that the HFD group had a larger contribution of thicker blood vessels compared to the OLD group. Moreover, the high fat diet affected also the blood vessel network organization and branching (Fig. 6B–C). The average branch length increased significantly (1.2-fold; Fig. 6H), going together with a significant decrease in the number of branches (3.7-fold; Fig. 6G).

3.4. Bone pathology study - spatial relation between the different skeletal tissues within long bones

The novel contrast agent allowed 3D visualization, in one CE-CT dataset, of different skeletal tissues, namely mineralized bone, bone marrow adipocytes and bone marrow vasculature. Therefore, these different tissues could not only be analyzed individually, but also their spatial distribution, in 3D, within the tibial metaphysis as well as their relation to each other could be assessed. Fig. 7A–C presents the three different skeletal tissues and their spatial distribution. The adipocytes in the OLD and HFD group were not uniformly dispersed in the metaphysis, but mostly located in the medial area, with an additional tendency towards the lateral side in the HFD group. These data indicate that Hf-POM CE-CT can assess local changes in the bone marrow adipose tissue, which are not always easy to detect using histology.

Moreover, in HFD-fed mice the number of adipocytes in close vicinity to the bone (<8 μm) was decreased, whereas more adipocytes were located at larger distance from the bone (>64 μm; Fig. 7D). Aging did not alter the spatial distribution of adipocytes relative to the bone compared to the YNG group, even though the number of adipocytes was significantly larger. On the other hand, aging increased the average distance between the bone and the blood vessels significantly (Fig. 7E), whereas the high fat diet had no additional effect on this parameter.

To conclude, we summarized in Table 2 the benefits and disadvantages of histomorphometry and Hf-POM-based CE-CT, with respect to visualization and morphological quantification of mineralized bone, bone marrow adipocytes and vasculature. First, we would like to underscore that both techniques are highly complementary for assessing biological tissues. Histological analysis can provide (sub)cellular information when using cell-specific stains (TRAP for osteoclasts, osterix for skeletal cells, sclerostin for osteocytes, etc.) and imaging the histological sections at high spatial resolution. On the other hand, Hf-POM-based CE-CT analysis is less labor intensive, time-consuming and destructive compared to histomorphometry. Most importantly, it provides 3D visualization within the same dataset of the three skeletal tissues and allows analysis of their spatial relation.

4. Conclusions

In this study, we aimed to develop and validate a novel contrast agent for CE-CT, i.e. Hf-POM. We first gained a better

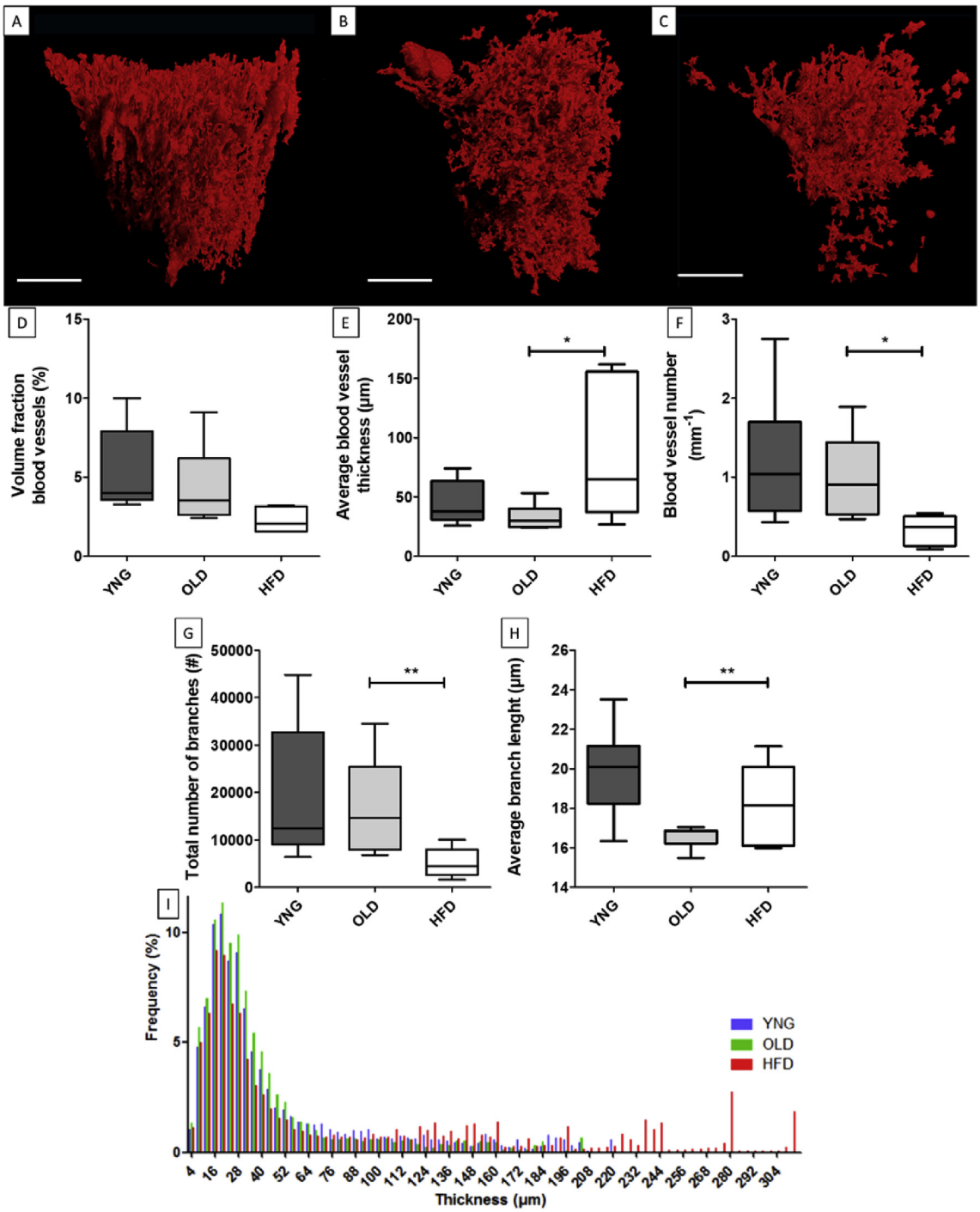

Fig. 6. Quantitative morphological assessment of the bone marrow vasculature. Representative 3D visualization, using Hf-POM-based CE-CT, of the blood vessel network in the bone marrow compartment of the tibial metaphysis of (A) YNG, (B) OLD and (C) HFD mice. Scale bars = 250 µm. Quantification of the (D) volume fraction of the blood vessels in the MV, (E) average blood vessel thickness, (F) blood vessel density, (G) total number of branches, (H) average branch length and (I) distribution of the blood vessel thickness for the YNG, OLD and HFD groups. $n = 7 - 8$ *per group.* $^{*}p < .05$ *and* $^{**}p < .01$. Apart from graph (I), all data are represented in a box plot as median ± min/max. The HFD group and YNG group were both independently compared to OLD animals by using a two-tailed unpaired *t*-test.

understanding of the binding mechanisms and affinity of the Hf-POM, and we assessed its non-destructiveness and its potential for soft tissue staining in murine long bones as blueprint. Our data shows that this new contrast agent allows 3D multi-tissue CE-CT imaging, without the need for perfusion, and can thus be used for virtual 3D histology. More specifically, Hf-POM-based CE-CT can reveal and characterize, in a single dataset, the 3D structure of different skeletal tissues (i.e. mineralized bone, adipocytes and blood vessels). Since it provides additional data to standard histomorphometry, with more spatial information, CE-CT can offer novel insights in the complex mechanisms of normal bone development and bone pathologies and will thus be highly valuable for *in vivo* screening of biomaterials for skeletal regeneration.

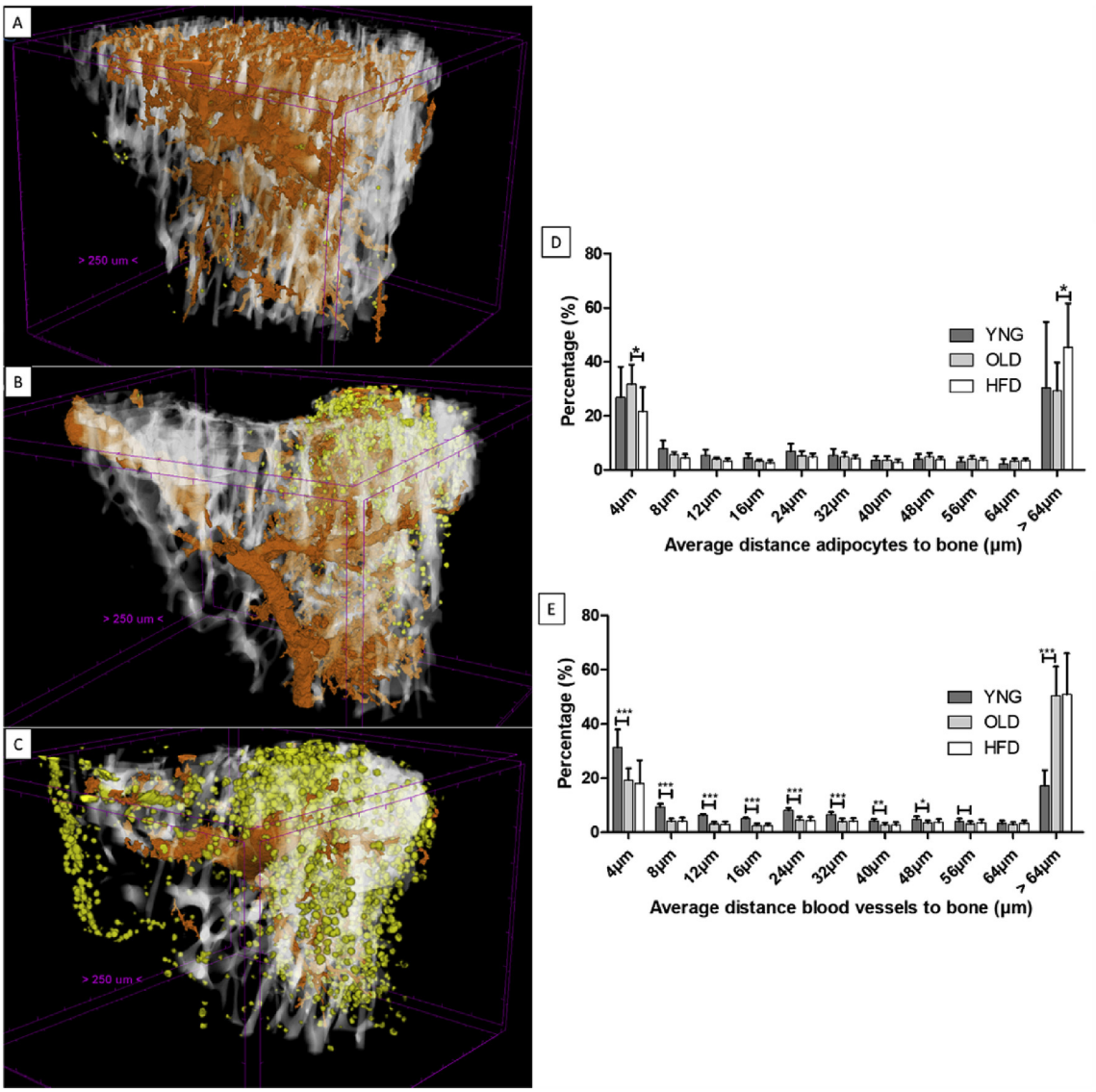

Fig. 7. Spatial relation of the different skeletal tissues within long bones. Representative 3D visualization, using Hf-POM-based CE-CT, of the trabecular bone (white), blood vessel network (orange) and adipocytes (yellow) in the tibial metaphysis of (A) YNG, (B) OLD and (C) HFD mice. 3D scale bars indicated in the image. CE-CT based histogram of the distance between (D) the adipocytes and the trabecular bone and (E) the blood vessels and the trabecular bone for the YNG, OLD and HFD groups Scale bars = 250 µm. Statistical comparison was made between YNG and OLD, and between OLD and HFD. $^{*}p < .05$, $^{**}p < .01$ and $^{***}p < .001$. Data are represented as mean + SD. The HFD group and YNG group were both independently compared to OLD animals by using a two-tailed unpaired *t*-test. (For interpretation of the references to color in this figure legend, the reader is referred to the Web version of this article.)

Table 2
Benefits and disadvantages of histomorphometry and Hf-POM-based CE-CT.

	Histomorphometry	Hf-POM-based CE-CT
Dimension of analysis	2D or 2D+ (serial sectioning or thick sections)	2D and 3D
Level of analysis	Subcellular, cellular and tissue level	Cellular and tissue level
Type of analysis	Quantitative and spatial (2D+ connectivity and distribution)	Quantitative and spatial (3D connectivity and distribution; interrelation and local distribution of the skeletal tissues)
Number of stainings needed to visualize bone, adipocytes and blood vessels	2–3	1
Duration of sample preparation, acquisition and analysis	4-5 weeks	2D analysis: 2 days 3D analysis: 1 week

Conflicts of interest

None.

Acknowledgements

We would like to acknowledge Karen Moermans and Riet Van Looveren for their valuable assistance in the histological processing of the samples. GK and SS are financed by a postdoctoral grant of the Research Foundation Flanders (FWO/12R4315N and FWO/12H5917N, respectively). NvG is funded by KUL-GOA grant 3M120209. GK and LG acknowledge support by the European Research Council under the European Union's Seventh Framework Program (FP7/2007-2013)/ERC grant agreement no. 279100. GC acknowledges support from the Research Foundation Flanders (FWO/G096414N). The CE-CT images have been generated at the X-ray computed tomography facilities of the Department of Materials Engineering and the Department of Development and Regeneration of the KU Leuven, both financed by the Hercules Foundation (project AKUL 09/001 and AKUL 13/47). This work is part of Prometheus, the Leuven Research & Development Division of Skeletal Tissue Engineering of the KU Leuven: www.kuleuven.be/prometheus.

Authors' roles: Study design: GK, NvG, AS, MD, GC. Study conduct: GK, SS, NvG, AS, GF. Data collection: GK, SS, NvG, AS, GF. Data analysis: GK, SS, NvG, AS, GF. Data interpretation: GK, SS, NvG, AS, GF, GP, LG, KV, TPV, GC. Drafting manuscript: GK, SS, GF, TPV, GC. Revising manuscript content: GK, SS, NvG, AS, GF, GP, MD, FL, LG, KV, TPV, GC. Approving final version of manuscript: GK, SS, NvG, AS, GF, GP, MD, FL, LG, KV, TPV, GC. GK takes full responsibility for the integrity of the data analysis.

Appendix A. Supplementary data

Supplementary data related to this article can be found at https://doi.org/10.1016/j.biomaterials.2017.12.016.

References

[1] C. Nombela-Arrieta, G. Pivarnik, B. Winkel, K.J. Canty, B. Harley, J.E. Mahoney, S.Y. Park, J. Lu, A. Protopopov, L.E. Silberstein, Quantitative imaging of haematopoietic stem and progenitor cell localization and hypoxic status in the bone marrow microenvironment, Nat. Cell Biol. 15 (5) (2013) 533–543.
[2] A.P. Kusumbe, S.K. Ramasamy, A. Starsichova, R.H. Adams, Sample preparation for high-resolution 3D confocal imaging of mouse skeletal tissue, Nat. Protoc. 10 (12) (2015) 1904–1914.
[3] I. Kallai, O. Mizrahi, W. Tawackoli, Z. Gazit, G. Pelled, D. Gazit, Microcomputed tomography-based structural analysis of various bone tissue regeneration models, Nat. Protoc. 6 (1) (2011) 105–110.
[4] M.L. Bouxsein, S.K. Boyd, B.A. Christiansen, R.E. Guldberg, K.J. Jepsen, R. Muller, Guidelines for assessment of bone microstructure in rodents using micro-computed tomography, J. Bone Mineral Res. Off. J. Am. Soc. Bone Mineral Res. 25 (7) (2010) 1468–1486.
[5] G. Kerckhofs, Y.C. Chai, F.P. Luyten, L. Geris, Combining microCT-based characterization with empirical modelling as a robust screening approach for the design of optimized CaP-containing scaffolds for progenitor cell-mediated bone formation, Acta Biomater. 35 (2016) 330–340.
[6] B. Lecka-Czernik, Marrow fat metabolism is linked to the systemic energy metabolism, Bone 50 (2) (2012) 534–539.
[7] M.J. Devlin, C.J. Rosen, The bone-fat interface: basic and clinical implications of marrow adiposity, Lancet Diabetes Endo 3 (2) (2015) 141–147.
[8] R.D. Prisby, Bone marrow blood vessel ossification and "microvascular dead space" in rat and human long bone, Bone 64 (2014) 195–203.
[9] M. Marenzana, T. Arnett, The key role of the blood supply to bone, Bone Res. 1 (2013) 203–215.
[10] M.G. Bixel, A.P. Kusumbe, S.K. Ramasamy, K.K. Sivaraj, S. Butz, D. Vestweber, R.H. Adams, Flow dynamics and HSPC homing in bone marrow microvessels, Cell Rep. 18 (7) (2017) 1804–1816.
[11] S. Stegen, N. van Gastel, G. Carmeliet, Bringing new life to damaged bone: the importance of angiogenesis in bone repair and regeneration, Bone 70 (2015) 19–27.
[12] D.P. Cormode, P.C. Naha, Z.A. Fayad, Nanoparticle contrast agents for computed tomography: a focus on micelles, Contrast Media Mol. Imaging 9 (1) (2014) 37–52.
[13] H. Lusic, M.W. Grinstaff, X-ray-computed tomography contrast agents, Chem. Rev. 113 (3) (2013) 1641–1666.
[14] C.L. Duvall, W.R. Taylor, D. Weiss, R.E. Guldberg, Quantitative microcomputed tomography analysis of collateral vessel development after ischemic injury, Am. J. Physiol. Heart Circ. Physiol. 287 (1) (2004) H302–H310.
[15] H. Nyangoga, P. Mercier, H. Libouban, M.F. Basle, D. Chappard, Three-dimensional characterization of the vascular bed in bone metastasis of the rat by microcomputed tomography (MicroCT), PLoS One 6 (3) (2011), e17336.
[16] M.H. Lafage-Proust, B. Roche, M. Langer, D. Cleret, A. Vanden Bossche, T. Olivier, L. Vico, Assessment of bone vascularization and its role in bone remodeling, BoneKEy Rep. 4 (2015) 662.
[17] R. Prisby, A. Guignandon, A. Vanden-Bossche, F. Mac-Way, M.T. Linossier, M. Thomas, N. Laroche, L. Malaval, M. Langer, Z.A. Peter, F. Peyrin, L. Vico, M.H. Lafage-Proust, Intermittent PTH(1-84) is osteoanabolic but not osteoangiogenic and relocates bone marrow blood vessels closer to bone-forming sites, J. Bone Miner. Res. 26 (11) (2011) 2583–2596.
[18] J.D. Boerckel, D.E. Mason, A.M. McDermott, E. Alsberg, Microcomputed tomography: approaches and applications in bioengineering, Stem Cell Res. Ther. 5 (6) (2014) 144.
[19] M. Sonnaert, G. Kerckhofs, I. Papantoniou, S. Van Vlierberghe, V. Boterberg, P. Dubruel, F.P. Luyten, J. Schrooten, L. Geris, Multifactorial optimization of contrast-enhanced nanofocus computed tomography for quantitative analysis of Neo-tissue formation in tissue engineering constructs, PLoS One 10 (6) (2015), e0130227.
[20] L. Xie, A.S.P. Lin, R.E. Guldberg, M.E. Levenston, Nondestructive assessment of sGAG content and distribution in normal and degraded rat articular cartilage via EPIC-mu CT, Osteoarthritis Cartilage 18 (1) (2010) 65–72.
[21] B.A. Lakin, D.J. Grasso, S.S. Shah, R.C. Stewart, P.N. Bansal, J.D. Freedman, M.W. Grinstaff, B.D. Snyder, Cationic agent contrast-enhanced computed tomography imaging of cartilage correlates with the compressive modulus and coefficient of friction, Osteoarthritis Cartilage 21 (1) (2013) 60–68.
[22] T.S. Silvast, J.S. Jurvelin, V. Tiitu, T.M. Quinn, J. Töyräs, Bath concentration of anionic contrast agents does not affect their diffusion and distribution in articular cartilage in Vitro, Cartilage 4 (1) (2013) 42–51.
[23] G. Kerckhofs, J. Sainz, M. Marechal, M. Wevers, T. Van de Putte, L. Geris, J. Schrooten, Contrast-enhanced nanofocus X-ray computed tomography allows virtual three-dimensional histopathology and morphometric analysis of osteoarthritis in small animal models, Cartilage 5 (1) (2014) 55–65.
[24] R.C. Stewart, P.N. Bansal, V. Entezari, H. Lusic, R.M. Nazarian, B.D. Snyder, M.W. Grinstaff, Contrast-enhanced CT with a high-affinity cationic contrast agent for imaging ex vivo bovine, intact ex vivo rabbit, and in vivo rabbit cartilage, Radiology 266 (1) (2013) 141–150.
[25] L.N. Hayward, C.M. de Bakker, L.C. Gerstenfeld, M.W. Grinstaff, E.F. Morgan, Assessment of contrast-enhanced computed tomography for imaging of cartilage during fracture healing, J. Orthop. Res. 31 (4) (2013) 567–573.
[26] S.S. Karhula, M.A. Finnila, M.J. Lammi, J.H. Ylarinne, S. Kauppinen, L. Rieppo, K.P. Pritzker, H.J. Nieminen, S. Saarakkala, Effects of articular cartilage constituents on phosphotungstic acid enhanced micro-computed tomography, PLoS One 12 (1) (2017), e0171075.
[27] H.J. Nieminen, H.K. Gahunia, K.P.H. Pritzker, T. Ylitalo, L. Rieppo, S.S. Karhula, P. Lehenkari, E. Haeggstrom, S. Saarakkala, 3D histopathological grading of osteochondral tissue using contrast-enhanced micro-computed tomography, Osteoarthritis Cartilage 25 (10) (2017) 1680–1689.
[28] H.J. Nieminen, T. Ylitalo, S. Karhula, J.P. Suuronen, S. Kauppinen, R. Serimaa, E. Haeggstrom, K.P. Pritzker, M. Valkealahti, P. Lehenkari, M. Finnila, S. Saarakkala, Determining collagen distribution in articular cartilage using contrast-enhanced micro-computed tomography, Osteoarthritis Cartilage 23 (9) (2015) 1613–1621.
[29] M. Styner, W.R. Thompson, K. Galior, G. Uzer, X. Wu, S. Kadari, N. Case, Z.H. Xie, B. Sen, A. Romaine, G.M. Pagnotti, C.T. Rubin, M.A. Styner, M.C. Horowitz, J. Rubin, Bone marrow fat accumulation accelerated by high fat diet is suppressed by exercise, Bone 64 (2014) 39–46.
[30] E.L. Scheller, C.R. Doucette, B.S. Learman, W.P. Cawthorn, S. Khandaker, B. Schell, B. Wu, S.Y. Ding, M.A. Bredella, P.K. Fazeli, B. Khoury, K.J. Jepsen, P.F. Pilch, A. Klibanski, C.J. Rosen, O.A. MacDougald, Region-specific variation in the properties of skeletal adipocytes reveals regulated and constitutive marrow adipose tissues, Nat. Commun. 6 (2015) 7808.
[31] E.L. Scheller, N. Troiano, J.N. Vanhoutan, M.A. Bouxsein, J.A. Fretz, Y. Xi, T. Nelson, G. Katz, R. Berry, C.D. Church, C.R. Doucette, M.S. Rodeheffer, O.A. Macdougald, C.J. Rosen, M.C. Horowitz, Use of osmium tetroxide staining with microcomputerized tomography to visualize and quantify bone marrow adipose tissue in vivo, Meth. Enzymol. 537 (2014) 123–139.
[32] B.D. Metscher, MicroCT for comparative morphology: simple staining methods allow high-contrast 3D imaging of diverse non-mineralized animal tissues, BMC Physiol. 9 (2009) 11.
[33] M.D. Wong, A.E. Dorr, J.R. Walls, J.P. Lerch, R.M. Henkelman, A novel 3D mouse embryo atlas based on micro-CT, Development 139 (17) (2012) 3248–3256.
[34] P. Vickerton, J. Jarvis, N. Jeffery, Concentration-dependent specimen shrinkage in iodine-enhanced microCT, J. Anat. 223 (2) (2013) 185–193.
[35] J. Buytaert, J. Goyens, D. De Greef, P. Aerts, J. Dirckx, Volume shrinkage of bone, brain and muscle tissue in sample preparation for micro-CT and light sheet fluorescence microscopy (LSFM), Microscopy and microanalysis : the official journal of Microscopy Society of America, Microbeam Analysis Society, Microsc. Soc. Canada 20 (4) (2014) 1208–1217.

[36] T. Schulz-Mirbach, M. Hess, B.D. Metscher, Sensory epithelia of the fish inner ear in 3D: studied with high-resolution contrast enhanced microCT, Front. Zool. 10 (1) (2013) 63.
[37] E. Pauwels, D. Van Loo, P. Cornillie, L. Brabant, L. Van Hoorebeke, An exploratory study of contrast agents for soft tissue visualization by means of high resolution X-ray computed tomography imaging, J. Microsc. 250 (1) (2013) 21–31.
[38] D. Farcasiu, J.Q. Li, Acidity measurements on a heteropolyacid hydrate in acetic-acid solution - a case of 3 hydrons ionizing independently, rather than consecutively, J. Catal. 152 (1) (1995) 198–203.
[39] J. Ye, C. Wu, Immobilization of polyoxometalates in crystalline solids for highly efficient, Dalton Trans. 45 (25) (2016) 10101–10112.
[40] S. Vanhaecht, G. Absillis, T. Parac-Vogt, Hydrolysis of DNA model substrates catalyzed by metal-substituted Wells-Dawson, Dalton Trans. 41 (33) (2012) 10028–10034.
[41] A. Sap, G. Absillis, T. Parac-Vogt, - Selective hydrolysis of oxidized insulin chain B by a Zr(IV)-substituted, Dalton Trans. 44 (4) (2015) 1539–1548.
[42] T. Pascart, G. Falgayrac, H. Migaud, J.F. Quinchon, L. Norberciak, J.F. Budzik, J. Paccou, A. Cotten, G. Penel, B. Cortet, Region specific Raman spectroscopy analysis of the femoral head reveals that trabecular bone is unlikely to contribute to non-traumatic osteonecrosis, Sci. Rep. 7 (1) (2017) 97.
[43] C. Olejnik, G. Falgayrac, A. During, B. Cortet, G. Penel, Doses effects of zoledronic acid on mineral apatite and collagen quality of newly-formed bone in the rat's calvaria defect, Bone 89 (2016) 32–39.
[44] G.S. Mandair, M.D. Morris, Contributions of Raman spectroscopy to the understanding of bone strength, BoneKEy Rep. 4 (2015) 620.
[45] A. Masic, L. Bertinetti, R. Schuetz, L. Galvis, N. Timofeeva, J.W. Dunlop, J. Seto, M.A. Hartmann, P. Fratzl, Observations of multiscale, stress-induced changes of collagen orientation in tendon by polarized Raman spectroscopy, Biomacromolecules 12 (11) (2011) 3989–3996.
[46] G. Kerckhofs, M. Durand, R. Vangoitsenhoven, C. Marin, B. Van der Schueren, G. Carmeliet, F.P. Luyten, L. Geris, K. Vandamme, Changes in bone macro- and microstructure in diabetic obese mice revealed by high resolution microfocus X-ray computed tomography, Sci. Rep. 6 (2016) 35517.
[47] S. Stegen, N. van Gastel, G. Eelen, B. Ghesquiere, F. D'Anna, B. Thienpont, J. Goveia, S. Torrekens, R. Van Looveren, F. Luyten, P. Maxwell, B. Wielockx, D. Lambrechts, S. Fendt, P. Carmeliet, G. Carmeliet, HIF-1alpha promotes glutamine-mediated redox homeostasis and glycogen-dependent, Cell Metabol. 23 (2) (2016) 265–279.
[48] N. van Gastel, S. Torrekens, S. Roberts, K. Moermans, J. Schrooten, P. Carmeliet, A. Luttun, F. Luyten, G. Carmeliet, Engineering vascularized bone: osteogenic and proangiogenic potential of murine, Stem Cell. 30 (11) (2012) 2460–2471.
[49] G. Kerckhofs, J. Schrooten, T. Van Cleynenbreugel, S.V. Lomov, M. Wevers, Validation of x-ray microfocus computed tomography as an imaging tool for porous structures, Rev. Sci. Instrum. 79 (1) (2008), 013711–013711-9.
[50] T. Hildebrand, P. Ruegsegger, A new method for the model-independent assessment of thickness in three-dimensional images, J Microsc-Oxford 185 (1997) 67–75.
[51] M. Doube, M.M. Klosowski, I. Arganda-Carreras, F.P. Cordelieres, R.P. Dougherty, J.S. Jackson, B. Schmid, J.R. Hutchinson, S.J. Shefelbine, BoneJ: free and extensible bone image analysis in ImageJ, Bone 47 (6) (2010) 1076–1079.
[52] G. Bertrand, G. Malandain, A note on building skeleton models via 3-D medial surface Axis thinning algorithms, Graph. Model. Image Process. 57 (6) (1995) 537–538.
[53] T.C. Lee, R.L. Kashyap, C.N. Chu, Building skeleton models via 3-D medial surface Axis thinning algorithms, Cvgip-Graph Model Im 56 (6) (1994) 462–478.
[54] J. Schindelin, I. Arganda-Carreras, E. Frise, V. Kaynig, M. Longair, T. Pietzsch, S. Preibisch, C. Rueden, S. Saalfeld, B. Schmid, J.Y. Tinevez, D.J. White, V. Hartenstein, K. Eliceiri, P. Tomancak, A. Cardona, Fiji: an open-source platform for biological-image analysis, Br. J. Pharmacol. 9 (7) (2012) 676–682.
[55] C. Kumar, N. Rambabu, N. Lingaiah, P. Prasad, A. Dalai, Hafnium salts of dodeca-tungstophosphoric acid catalysts for liquid phase benzylation of anisole with dibenzylether, Appl. Catal. Gen. 471 (2014) 1–11.
[56] C. Rocchiccioliдeltcheff, R. Thouvenot, R. Franck, IR and Raman-spectra of alpha-XM12O40N- heteropolyanions with keggin type structure (X = BIII, SIIV, GEIV, PV, ASV AND M = WVI AND MOVI, Spectrochim. Acta Mol. Biomol. Spectrosc. 32 (3) (1976) 587–597.
[57] C.R. Kumar, N. Rambabu, N. Lingaiah, P.S.S. Prasad, A.K. Dalai, Hafnium salts of dodeca-tungstophosphoric acid catalysts for liquid phase benzylation of anisole with dibenzylether, Appl. Catal. Gen. 471 (2014) 1–11.
[58] L. Galvis, J.W. Dunlop, G. Duda, P. Fratzl, A. Masic, Polarized Raman anisotropic response of collagen in tendon: towards 3D orientation mapping of collagen in tissues, PLoS One 8 (5) (2013), e63518.
[59] E. Gentleman, R.J. Swain, N.D. Evans, S. Boonrungsiman, G. Jell, M.D. Ball, T.A. Shean, M.L. Oyen, A. Porter, M.M. Stevens, Comparative materials differences revealed in engineered bone as a function of cell-specific differentiation, Nat. Mater. 8 (9) (2009) 763–770.
[60] M. Guilbert, G. Said, T. Happillon, V. Untereiner, R. Garnotel, P. Jeannesson, G.D. Sockalingum, Probing non-enzymatic glycation of type I collagen: a novel approach using Raman and infrared biophotonic methods, Biochim. Biophys. Acta 1830 (6) (2013) 3525–3531.
[61] G. McLaughlin, I.K. Lednev, A modified Raman multidimensional spectroscopic signature of blood to account for the effect of laser power, Forensic Sci. Int. 240 (2014) 88–94.
[62] K. Narasimhan, S. Pillay, N.R. Bin Ahmad, Z. Bikadi, E. Hazai, L. Yan, P.R. Kolatkar, K. Pervushin, R. Jauch, Identification of a polyoxometalate inhibitor of the DNA binding activity of Sox2, ACS Chem. Biol. 6 (6) (2011) 573–581.
[63] J.J. Cao, B.R. Gregoire, H. Gao, High-fat diet decreases cancellous bone mass but has no effect on cortical bone mass in the tibia in mice, Bone 44 (6) (2009) 1097–1104.
[64] B. Lecka-Czernik, L.A. Stechschulte, P.J. Czernik, A.R. Dowling, High bone mass in adult mice with diet-induced obesity results from a combination of initial increase in bone mass followed by attenuation in bone formation; implications for high bone mass and decreased bone quality in obesity, Mol. Cell. Endocrinol. 410 (2015) 35–41.
[65] R.L. Jilka, The relevance of mouse models for investigating age-related bone loss in humans, J Gerontol a-Biol 68 (10) (2013) 1209–1217.
[66] M.D. Willinghamm, M.D. Brodt, K.L. Lee, A.L. Stephens, J. Ye, M.J. Silva, Age-related changes in bone structure and strength in female and male BALB/c mice, Calcif. Tissue Int. 86 (6) (2010) 470–483.
[67] J.A. Inzana, M. Kung, L. Shu, D. Hamada, L.P. Xing, M.J. Zuscik, H.A. Awad, R.A. Mooney, Immature mice are more susceptible to the detrimental effects of high fat diet on cancellous bone in the distal femur, Bone 57 (1) (2013) 174–183.
[68] Y. Fujita, K. Watanabe, K. Maki, Serum leptin levels negatively correlate with trabecular bone mineral density in high-fat diet-induced obesity mice, J. Musculoskelet. Neuronal Interact. 12 (2) (2012) 84–94.
[69] H. Fehrendt, T. Linn, S. Hartmann, G. Szalay, C. Heiss, R. Schnettler, K.S. Lips, Negative influence of a long-term high-fat diet on murine bone architecture, Int. J. Endocrinol. 2014 (2014) 318924.
[70] C.R. Doucette, M.C. Horowitz, R. Berry, O.A. MacDougald, R. Anunciado-Koza, R.A. Koza, C.J. Rosen, A high fat diet increases bone marrow adipose tissue (MAT) but does not alter trabecular or cortical bone mass in C57BL/6J mice, J. Cell. Physiol. 230 (9) (2015) 2032–2037.
[71] L. Shu, E. Beier, T. Sheu, H. Zhang, M.J. Zuscik, E.J. Puzas, B.F. Boyce, R.A. Mooney, L. Xing, High-fat diet causes bone loss in young mice by promoting osteoclastogenesis through alteration of the bone marrow environment, Calcif. Tissue Int. 96 (4) (2015) 313–323.
[72] O. Demontiero, W. Li, E. Thembani, G. Duque, Validation of noninvasive quantification of bone marrow fat volume with microCT in aging rats, Exp. Gerontol. 46 (6) (2011) 435–440.
[73] P. Hardouin, T. Rharass, S. Lucas, Bone marrow adipose tissue: to Be or not to Be a typical adipose tissue? Front. Endocrinol. 7 (2016) 85.
[74] M. Styner, W.R. Thompson, K. Galior, G. Uzer, X. Wu, S. Kadari, N. Case, Z. Xie, B. Sen, A. Romaine, G.M. Pagnotti, C.T. Rubin, M.A. Styner, M.C. Horowitz, J. Rubin, Bone marrow fat accumulation accelerated by high fat diet is suppressed by exercise, Bone 64 (2014) 39–46.
[75] E.L. Scheller, B. Khoury, K.L. Moller, N.K. Wee, S. Khandaker, K.M. Kozloff, S.H. Abrishami, B.F. Zamarron, K. Singer, Changes in skeletal integrity and marrow adiposity during high-fat diet and after weight loss, Front. Endocrinol. 7 (2016) 102.